

See discussions, stats, and author profiles for this publication at: <https://www.researchgate.net/publication/337834485>

Fabrication of Hollow CoP/TiO_x Heterostructures for Enhanced Oxygen Evolution Reaction

Article in *Small* · December 2019

DOI: 10.1002/sml.201905075

CITATIONS

2

READS

168

13 authors, including:



Zibin Liang

Peking University

70 PUBLICATIONS 2,065 CITATIONS

[SEE PROFILE](#)



Song Gao

Peking University

51 PUBLICATIONS 634 CITATIONS

[SEE PROFILE](#)



Ruo Zhao

Peking University

27 PUBLICATIONS 771 CITATIONS

[SEE PROFILE](#)



Hao Zhang

Peking University

22 PUBLICATIONS 97 CITATIONS

[SEE PROFILE](#)

Some of the authors of this publication are also working on these related projects:



energy storage [View project](#)



Carbon Supported Nanostructures for Electrocatalysis [View project](#)

Fabrication of Hollow CoP/TiO_x Heterostructures for Enhanced Oxygen Evolution Reaction

Zibin Liang, Wenyang Zhou, Song Gao, Ruo Zhao, Hao Zhang, Yanqun Tang, Jinqian Cheng, Tianjie Qiu, Bingjun Zhu, Chong Qu, Wenhan Guo, Qian Wang,* and Ruqiang Zou*

Transition-metal phosphides have flourished as promising candidates for oxygen evolution reaction (OER) electrocatalysts. Herein, it is demonstrated that the electrocatalytic OER performance of CoP can be greatly improved by constructing a hybrid CoP/TiO_x heterostructure. The CoP/TiO_x heterostructure is fabricated using metal–organic framework nanocrystals as templates, which leads to unique hollow structures and uniformly distributed CoP nanoparticles on TiO_x. The strong interactions between CoP and TiO_x in the CoP/TiO_x heterostructure and the conductive nature of TiO_x with Ti³⁺ sites endow the CoP–TiO_x hybrid material with high OER activity comparable to the state-of-the-art IrO₂ or RuO₂ OER electrocatalysts. In combination with theoretical calculations, this work reveals that the formation of CoP/TiO_x heterostructure can generate a pathway for facile electron transport and optimize the water adsorption energy, thus promoting the OER electrocatalysis.

candidates.^[4] Many strategies have been explored to improve the electrocatalytic OER performance of TMPs such as nanostructuring^[5] and incorporation of foreign metal sites.^[4a,c] However, there is still a large room for further improvement of the electrocatalytic OER performance of TMPs by more precise control of their structures and compositions.

Recently, hybrid materials constructed with different functional components have attracted great attentions for electrochemical applications benefitting from the combined advantages/features and the synergistic effect of the different components.^[6] For example, the synergistic effect on the interfaces between different components can optimize the electronic

structure of active sites for adsorption and activation of the reactant molecules and modify the reaction pathway or the configurations of reaction intermediates, leading to greatly promoted reaction kinetics and accelerated reaction rates.^[6e–g] For OER electrocatalysis, however, the design and fabrication of hybrid materials with interface structure are not well-explored because of the absence of an effective strategy for the synthesis of hybrid materials with strong interfacial effect for promoting the reaction kinetics.

Herein, motivated by the aforementioned considerations, we demonstrated the fabrication of CoP–TiO_x hybrid material with CoP/TiO_x heterostructure for OER electrocatalysis. The presented CoP–TiO_x hybrid material has unique porous hollow nanocage TiO_x morphology coupled with ultrafine CoP nanoparticles and abundant CoP/TiO_x interfaces. The porous hollow TiO_x nanocages with abundant Ti³⁺ sites can serve as conductive substrates and promote the electron transfer as well as facilitate the mass transport. The use of TiO_x as conductive substrate offer advantage of high stability and low cost, which is especially important for OER as the commonly used carbon substrate may undergo severe corrosion and decrease the Faradic efficiency at high positive potentials. Moreover, the strong interactions and synergistic effect between CoP and TiO_x in the CoP/TiO_x heterostructure resulted in fast pathway for electron transport and optimized water adsorption energy. As a consequence, the CoP–TiO_x hybrid material showed remarkable activity and durability for OER electrocatalysis in alkaline solution, which were superior to the individual CoP or TiO_x and

1. Introduction

Oxygen evolution reaction (OER) is a key process for various energy storage and conversion devices including rechargeable metal-air batteries and electrochemical water splitting.^[1] As a four-electron-involving reaction, OER is a complicated and sluggish process, which requires efficient electrocatalysts to promote the kinetics and reduce the overpotential.^[2] Currently, Ir/Ru-based materials are highly active electrocatalysts for OER. However, their high cost, scarcity, and poor durability greatly hinder their widespread applications for OER. Therefore, great efforts have been devoted to developing earth-abundant materials with high activity and durability for OER electrocatalysis.^[2a,3] Among the developed earth-abundant OER electrocatalysts, transition-metal phosphides (TMPs) have emerged as promising

Z. Liang, W. Zhou, Dr. S. Gao, Dr. R. Zhao, Dr. H. Zhang, Y. Tang, J. Cheng, T. Qiu, Dr. B. Zhu, Dr. C. Qu, Dr. W. Guo, Prof. Q. Wang, Prof. R. Zou
Beijing Key Laboratory for Theory and Technology of Advanced Battery Materials
Department of Materials Science and Engineering
College of Engineering
Peking University
Beijing 100871, P. R. China
E-mail: qianwang2@pku.edu.cn; rzou@pku.edu.cn

The ORCID identification number(s) for the author(s) of this article can be found under <https://doi.org/10.1002/smll.201905075>.

DOI: 10.1002/smll.201905075

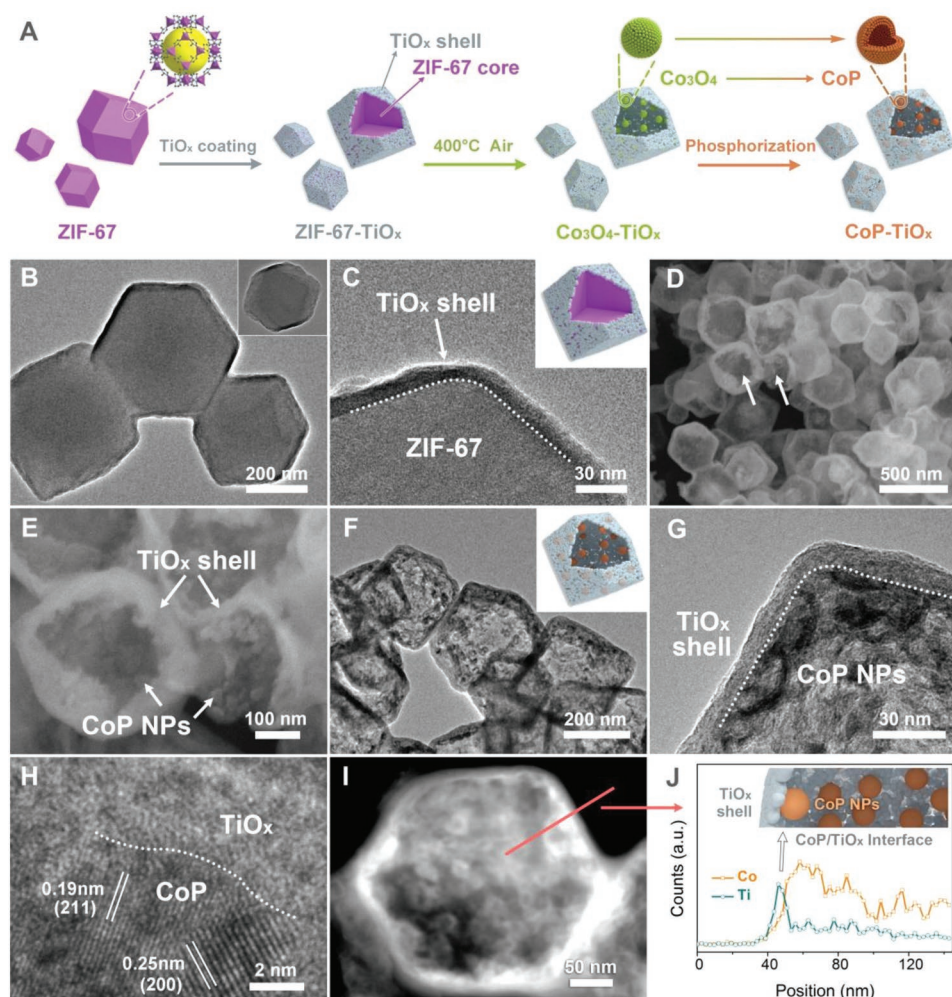


Figure 1. A) Schematic illustration of the fabrication of CoP–TiO_x hybrid hollow materials. B) TEM image of ZIF-67–TiO_x. Inset shows an isolated ZIF-67–TiO_x particle. C) TEM image of ZIF-67–TiO_x showing a thin TiO_x shell on the ZIF-67 core. Inset shows a schematic model of the core–shell ZIF-67–TiO_x structure. D) SEM image of CoP–TiO_x with arrows pointing to broken particles that shows hollow structure. E) SEM image of CoP–TiO_x showing the CoP nanoparticles distributed on the internal surface of the TiO_x shell. F) TEM image of CoP–TiO_x. Inset shows the schematic model of CoP–TiO_x. G) TEM image of CoP–TiO_x showing the interface (dot line) between the TiO_x shell and CoP nanoparticles. H) HRTEM image of CoP–TiO_x with dot line showing the CoP/TiO_x heterostructure. I) HAADF-STEM image and J) the corresponding EDS line-scan profile of CoP–TiO_x showing the CoP/TiO_x interface.

were comparable to the state-of-the-art IrO₂ and RuO₂ electrocatalysts. In combination with theoretical calculations based on density functional theory (DFT), we demonstrated the strong interactions between CoP and TiO_x in the CoP/TiO_x heterostructure play important role on its high electrochemical performance. This work not only presented a promising electrocatalyst for OER, but also explored a new strategy to improve OER performance through heterostructure construction and interface engineering.

2. Results and Discussion

The fabrication process of CoP–TiO_x was schematically illustrated in **Figure 1A**. Co-based metal–organic framework (MOF) nanocrystals, namely, ZIF-67 were first synthesized through the coprecipitation reaction of Co²⁺ and 2-methylimidazole

(Figure S1, Supporting Information).^[7] Transmission electron microscopy (TEM) images, X-ray diffraction (XRD) patterns, and N₂ sorption measurements confirmed the successful synthesis of ZIF-67 nanocrystals with particle size of ≈300 nm (Figure S1B–F, Supporting Information). Afterward, the ZIF-67 nanocrystals were uniformly coated with thin TiO_x shells through the hydrolysis, oligomerization, and condensation of titanium butoxide (see the Experimental Section).^[8] The ZIF-67 crystal structure of the resultant ZIF-67–TiO_x remained intact after TiO_x coating, and the absence of XRD peaks of crystalline TiO_x suggested the amorphous nature of the TiO_x shells (Figure S2, Supporting Information). TEM images of ZIF-67–TiO_x confirmed that the rhombic dodecahedron morphology of ZIF-67 was maintained while rough TiO_x shells with thickness of ≈15 nm that uniformly coat the ZIF-67 nanocrystals can be clearly recognized (Figure 1B,C). ZIF-67–TiO_x was then annealed at 400 °C in air to obtain Co₃O₄–TiO_x

(Figure S3, Supporting Information). The complete decomposition of ZIF-67 and formation of Co_3O_4 nanoparticles was confirmed by the disappeared ZIF-67 peaks and well-defined Co_3O_4 peaks in the XRD pattern of $\text{Co}_3\text{O}_4\text{-TiO}_x$ (Figure S3B, Supporting Information). The TiO_x shells were well maintained in $\text{Co}_3\text{O}_4\text{-TiO}_x$ and exhibited hollow nanocage structure as the ZIF-67 core completely decomposed into Co_3O_4 nanoparticles that were uniformly distributed on the internal surface of the TiO_x nanocages (Figures S3C,D and S4, Supporting Information). After phosphorization, the Co_3O_4 nanoparticles were in situ converted to CoP nanoparticles and the final product CoP- TiO_x was obtained. For comparison, Co_3O_4 and CoP were also synthesized from ZIF-67 nanocrystals without TiO_x shells (Figure S5, Supporting Information).

XRD pattern of CoP- TiO_x proved the complete transformation from Co_3O_4 into CoP (Figure S6, Supporting Information). CoP- TiO_x possessed hollow rhombic dodecahedron structure, with CoP nanoparticles uniformly distributed on the internal surface of the TiO_x nanocages (Figure 1D,E; Figure S7, Supporting Information). The TiO_x nanocages of CoP- TiO_x are porous and disordered (Figure S8, Supporting Information), and the CoP nanoparticles were showed to have hollow structure, which was formed because of the nanoscale Kirkendall effect (Figure 1F).^[9] The pore structure of CoP- TiO_x was investigated by nitrogen sorption measurements, which demonstrated the presence of meso/macropores in CoP- TiO_x (Figure S9, Supporting Information). These CoP hollow nanoparticles had an intimate contact with the TiO_x shells, leading to formation of abundant CoP/ TiO_x interface in CoP- TiO_x (Figure 1G). The CoP/ TiO_x interface was further demonstrated in high-resolution TEM (HRTEM) image, which clearly showed lattice fringes with spacings of 0.19 and 0.25 nm corresponding to the (211) and (200) planes of CoP, respectively, and the amorphous nature of the TiO_x shells (Figure 1H). Figure 1I,J illustrates the high-angle annular dark-field scanning TEM (HAADF-STEM) image of CoP- TiO_x and the corresponding energy-dispersive X-ray spectroscopy (EDS) line-scan profiles, which further confirmed the intimate contact between CoP and TiO_x and the existence of CoP/ TiO_x interface. Recently, precise synthesis and tuning of the heterojunction interface between two different components have been proven an efficient strategy to boost the electrocatalytic activity.^[6f,10] Remarkably, Zhang and co-workers demonstrated the NiO/ TiO_x interface can lead to facile electron transport and electron donation from NiO to TiO_x , resulting in enhanced electrocatalytic OER performance.^[10c] In this regard, it was expected that the existence of abundant CoP/ TiO_x interface can endow CoP- TiO_x with outstanding electrocatalytic OER activity because of the facilitated electron transport and the charge modification on the CoP/ TiO_x interface.

The existence of Co, P, Ti, O, and impurity C in CoP- TiO_x were confirmed by the XPS full spectrum, while those of $\text{Co}_3\text{O}_4\text{-TiO}_x$ and CoP showed the absence of P and Ti, respectively (Figure 2A). In high resolution P 2p spectrum of CoP- TiO_x , two peaks at 130.3 and 129.3 eV can be resolved, which can be assigned to P 2p_{1/2} and P 2p_{3/2} of CoP, respectively, along with a peak at 134.0 eV originated from oxidized phosphorus species (Figure 2B).^[11] High-resolution Co 2p spectrum of CoP- TiO_x consisted of peaks at 793.0 and 778.2 eV corresponding to Co 2p_{1/2} and 2p_{3/2} of CoP, respectively, as well as

peaks at 797.7 and 781.6 eV with two shakeup satellite peaks assigned to oxidized cobalt species (Figure 2C).^[4a,12] In contrast, the high-resolution Co 2p spectrum of $\text{Co}_3\text{O}_4\text{-TiO}_x$ only showed peaks of Co_3O_4 . In high-resolution Ti 2p spectrum, characteristic peaks for both Ti^{4+} (464.5 and 458.8 eV) and Ti^{3+} (464.0 and 458.2 eV) were observed, confirming the existence of abundant Ti^{3+} sites in the TiO_x shells (Figure 2D).^[10c] It has been reported that the existence of Ti^{3+} sites in TiO_x can greatly increase the charge carriers and the electrical conductivity.^[13] In this regard, the TiO_x shells of CoP- TiO_x with abundant Ti^{3+} sites was expected to serve as conductive substrates to facilitate the electron transport, leading to enhanced electrocatalytic OER performance. Interestingly, the high-resolution Co 2p and P 2p spectra exhibited that the CoP peaks of CoP- TiO_x had obvious binding energy shifts compared with CoP, indicating a charge transfer and strong interaction between CoP and TiO_x (Figure 2E,F). Specifically, the Co 2p peaks exhibited a negative binding energy shift of 0.51 eV and the P 2p peaks also had negative shifts of 0.39 and 0.36 eV for P 2p_{1/2} and P 2p_{3/2} peaks, respectively. The charge transfer and strong interaction between CoP and TiO_x are expected to modify the electronic structure of the active sites and promote the OER electrocatalytic kinetics.

Electrocatalytic OER experiments were carried out in a three-electrode configuration with 1 M KOH as electrolyte, and glassy carbon electrodes modified with catalysts ($\approx 0.2 \text{ mg cm}^{-2}$) were used as working electrodes. All the linear sweep voltammetry (LSV) curves were corrected with 95% iR compensation (Figure S10, Supporting Information). RuO_2 and IrO_2 nanoparticles were fabricated as reference materials to evaluate the OER performance of the samples (Figure S11, Supporting Information). The LSV curves normalized by the geometrical area of electrode (0.19625 cm^2) of different materials tested at a rotation rate of 1600 rpm were illustrated in Figure 3A. A dramatically increased anodic current density with onset potential of 1.50 V was observed for CoP- TiO_x , which was lower than those of CoP (1.52 V) and TiO_x (1.66 V), demonstrating a much enhanced electrocatalytic OER performance of CoP- TiO_x compared with the individual CoP and TiO_x . In addition to onset potential, overpotential at 10 mA cm^{-2} can be obtained from the LSV curves as well. CoP- TiO_x had an overpotential of 337 mV at 10 mA cm^{-2} , which was lower than those of CoP and TiO_x , and was comparable to those of the state-of-the-art IrO_2 and RuO_2 catalysts. The catalytic kinetics of the catalysts was revealed by Tafel plots (Figure 3B). The Tafel plots showed that CoP- TiO_x has a Tafel slope of $72.1 \text{ mV decade}^{-1}$, which was much smaller than those of CoP and TiO_x and was comparable to those of the IrO_2 and RuO_2 catalysts, indicating superior OER catalytic kinetics for CoP- TiO_x . To minimize the influence of the different electrochemical surface area (ECSA) and to further compare the intrinsic OER activity of CoP- TiO_x , CoP, and TiO_x , their LSV curves were normalized by their ECSA. The ECSA was estimated by cycling the prepared electrodes in the non-Faradaic potential regions to get the electrical double-layer capacitances (C_{dl}) (Figure 3C). It showed that TiO_x had higher C_{dl} than that of CoP because of the porous nature of TiO_x , while their composites CoP- TiO_x exhibited a middle C_{dl} value. LSV curves of the samples were then normalized by ECSA based on the obtained C_{dl} values (see the Experimental Section). It demonstrated a OER activity

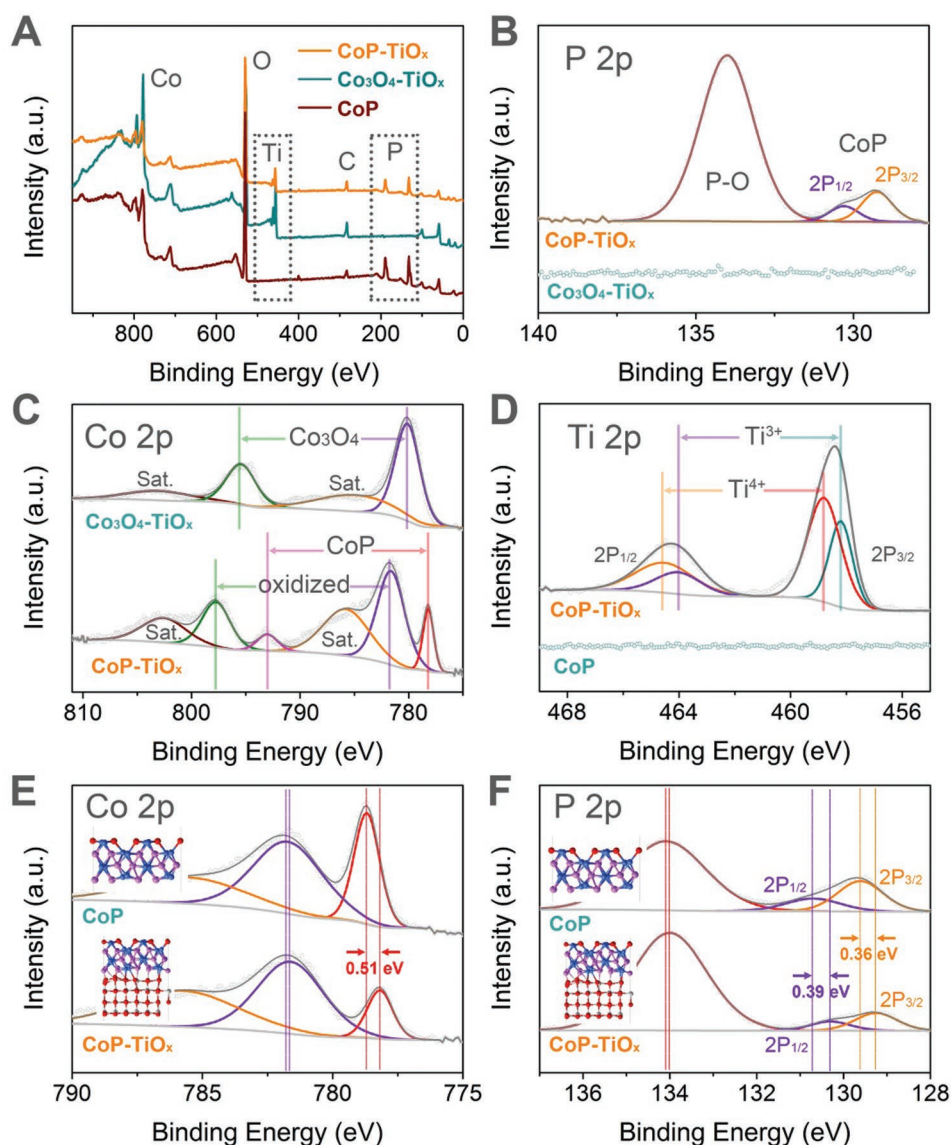


Figure 2. A) XPS full spectra of CoP-TiO_x, Co₃O₄-TiO_x, and CoP. B) High-resolution P 2p spectra of CoP-TiO_x and Co₃O₄-TiO_x. C) High-resolution Co 2p spectra of CoP-TiO_x and Co₃O₄-TiO_x. D) High-resolution Ti 2p spectra of CoP-TiO_x and CoP. High-resolution E) Co 2p and F) P 2p spectra of CoP-TiO_x and CoP demonstrating obvious binding energy shift after coupling CoP with TiO_x.

trend of CoP-TiO_x > CoP > TiO_x, similar to that based on geometrical area of electrode (Figure 3D). These results proved that CoP-TiO_x had much higher intrinsic OER activity compared with individual CoP or TiO_x, which can be attributed to the synergistic effect between CoP and TiO_x. To further prove the importance of the CoP/TiO_x, CoP-C-TiO_x without direct contact between CoP and TiO_x was fabricated by direct phosphorization of ZIF-67-TiO_x (Figure S12, Supporting Information). It showed that CoP-C-TiO_x exhibited poorer OER activity than CoP-TiO_x, which indicated the importance of the direct contact between CoP and TiO_x in the CoP/TiO_x interfaces for OER electrocatalysis. To prove the benefits of CoP-TiO_x for the formation of highly active sites, we fabricated Co₃O₄-TiO_x and Co(OH)₂-TiO_x as reference materials (Figure S13, Supporting Information). These cobalt-based materials are believed to have

similar active sites (e.g., cobalt oxyhydroxides) for OER electrocatalysis. CoP-TiO_x showed much higher current density and lower Tafel slope than those of Co₃O₄-TiO_x and Co(OH)₂-TiO_x, which demonstrated the superiority of CoP-TiO_x for formation of highly active sites for OER. Rotating ring-disk electrodes (RRDE) were used to confirm the exclusive O₂ production by CoP-TiO_x (Figures S14 and S15, Supporting Information). As demonstrated in Figure S15 (Supporting Information), a negligible current at ring electrode was observed even when a high current was detected at disk electrode, suggesting an ideal four-electron OER pathway (4OH⁻ = O₂ + 2H₂O + 4e⁻) with CoP-TiO_x as catalyst.^[14]

The durability measurements were carried out using carbon fiber papers with geometrical area of 1 cm² modified with catalysts as working electrodes as recommended in order to

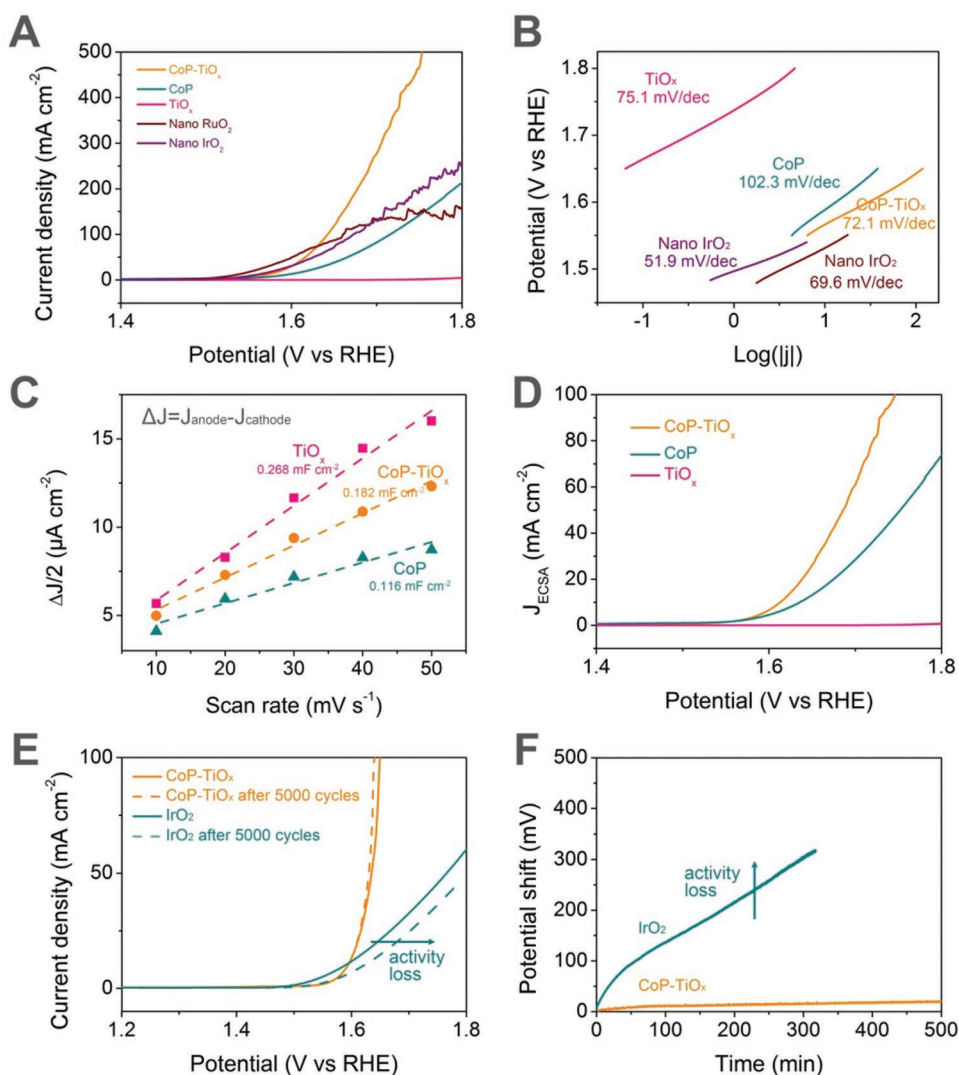


Figure 3. A) LSV curves and B) the corresponding Tafel plots of different catalysts normalized by the geometrical area of electrode (0.19625 cm^2). C) The capacitive current ($\Delta J/2$) as a function of scan rates for different catalysts to give the electrical double-layer capacitance. D) LSV curves of different catalysts normalized by electrochemical surface area. E) LSV curves of CoP-TiO_x and IrO₂ before and after cycling the potential between 1.4 and 1.6 V for 5000 cycles. F) Potential shifts at 10 mA cm^{-2} for carbon fiber papers of 1 cm^2 loaded with CoP-TiO_x or IrO₂.

reveal the available durability of the catalysts for large-scale water electrolysis.^[15] The catalytic durability of CoP-TiO_x was first evaluated by cycling the potential between 1.4 and 1.6 V for 5000 cycles (Figure 3E). LSV curves of CoP-TiO_x obtained before and after cycles exhibited negligible change, demonstrating a high durability of CoP-TiO_x for OER electrocatalysis. In contrast, the IrO₂ catalyst suffered from obvious activity loss after 5000 cycles. The high durability of CoP-TiO_x was further confirmed by chronopotentiometry measurement at 10 mA cm^{-2} (Figure 3F). Slight potential shift was obtained for CoP-TiO_x with only 19 mV potential increase at 10 mA cm^{-2} after 500 min, while the IrO₂ catalyst showed severe activity loss with potential shift of over 300 mV after 300 min. Both potential cycling tests and chronopotentiometry measurements revealed the superior durability of CoP-TiO_x for OER electrocatalysis. The outstanding activity and durability as well as its earth-abundant chemical composition made

CoP-TiO_x a promising OER electrocatalyst for large-scale water electrolysis.

It has been reported that the electrochemical OER activity of transition metal phosphides originated from the generation of a thin layer of oxides/oxyhydroxides on the surface of the phosphides. The oxides/oxyhydroxides layer provided abundant catalytically active sites for OER, while the phosphide core facilitated the electron transfer and the synergistic effect between the phosphide and the oxidized species may promote the OER kinetics.^[16] TEM and XPS measurements were carried out to elucidate the chemical composition and structure modification of CoP-TiO_x after the chronopotentiometry measurements. We found that the rhombic dodecahedron TiO_x shells remained almost intact and the HRTEM confirmed the existence of the CoP/TiO_x interface after long-term OER operation (Figure S16, Supporting Information). High-resolution XPS spectrum of Co 2p showed that the characteristic peaks for CoP (793.0 and

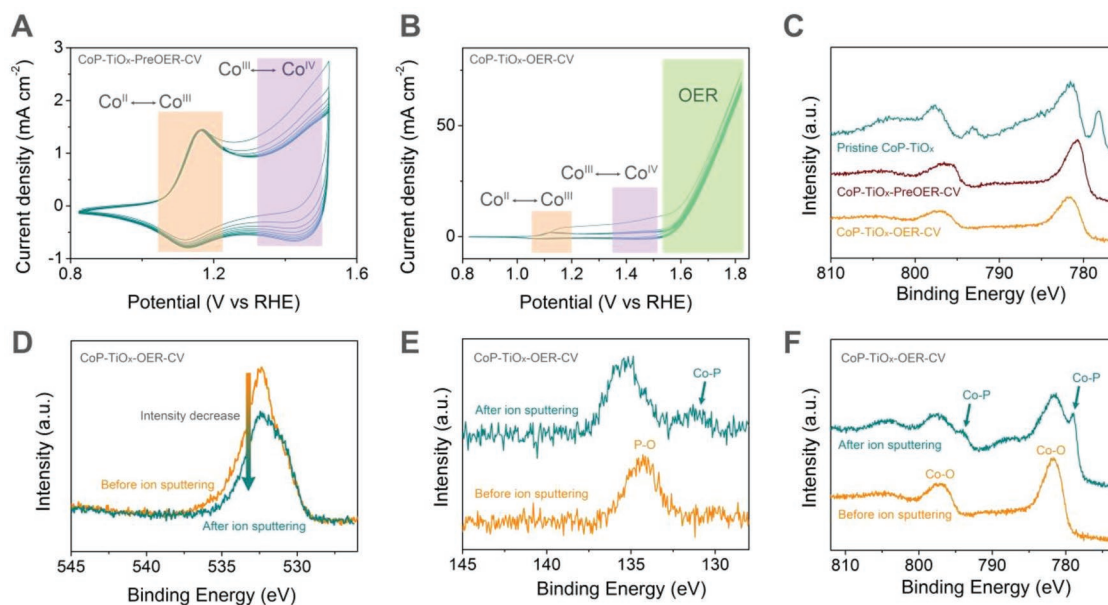


Figure 4. CV curves of the first ten cycles of CoP-TiO_x within A) pre-OER region and B) OER region. C) High-resolution XPS spectrum of Co 2p of CoP-TiO_x-PreOER-CV and CoP-TiO_x-OER-CV. High-resolution XPS spectrum of D) O 1s, E) P 2p, and F) Co 2p of CoP-TiO_x-OER-CV before and after argon ion sputtering.

778.2 eV) disappeared and the two peaks at 796.0 and 780.8 eV can be assigned to cobalt oxides/oxyhydroxides, indicating the oxidation of CoP and formation of cobalt oxides/oxyhydroxides on the surface of the CoP nanoparticles after chronopotentiometry measurements (Figure S17A, Supporting Information). For P 2p spectrum, the broad peak at 133.9 eV was attributed to the formation of phosphate species, which was corresponding to reported studies (Figure S17B, Supporting Information).^[16a] Moreover, the TiO_x nanocages remained intact in terms of the chemical composition according to the high-resolution XPS spectrum of Ti 2p. The Ti 2p spectrum confirmed the existence of abundant Ti³⁺ sites and negligible peak shift was detected after long-term OER operation (Figure S17C, Supporting Information). Both TEM and XPS measurements revealed the robust and stable nature of the TiO_x nanocages in CoP-TiO_x. To further investigate the structural/compositional evolution of CoP-TiO_x during OER process, we tested the CV curves of CoP-TiO_x within pre-OER region (Figure 4A, denoted as CoP-TiO_x-PreOER-CV) and OER region (Figure 4B, denoted as CoP-TiO_x-OER-CV) and tested their XPS signals. The CV curves of CoP-TiO_x showed redox peaks at around 1.1 and 1.4 V can be assigned to Co^{II}/Co^{III} and Co^{III}/Co^{IV} redox reactions, respectively.^[17] It has been demonstrated the pre-oxidation process of phosphides to form partially oxidized phosphides attributed to the OER performance of phosphides in alkaline solution.^[4c,16b,17,18] In our case, the high-resolution XPS spectrum of Co 2p of CoP-TiO_x-PreOER-CV and CoP-TiO_x-OER-CV showed similar peaks assigned to cobalt oxides/oxyhydroxides, which demonstrated that the surface of CoP in CoP-TiO_x was partially oxidized into cobalt oxides/oxyhydroxides in pre-OER potential region, which serve as the active sites for the subsequent OER electrocatalysis. To prove that the existent of CoP core, we applied argon ion sputtering to remove the oxidized surface of CoP-TiO_x-OER-CV and measured the XPS

signals of O 1s, P 2p, and Co 2p (Figure 4D-F). These results indicated the partially oxidized surface/CoP core structure was formed during OER, which was evidenced by the decrease intensity of O and appeared Co-P peaks after the oxidized surface was removed by argon ion sputtering.

The outstanding OER performance of CoP-TiO_x can be attributed to the following reasons: 1) the charge redistribution on the CoP/TiO_x interface may modify the electron density of CoP and thus the H₂O adsorption energy, leading to promoted OER kinetics.^[10c,19] The charge redistribution between CoP and TiO_x was evidenced by the binding energy shift of the CoP peaks in high-resolution Co 2p and P 2p spectra of CoP-TiO_x compared with CoP (Figure 2E,F). To further investigate the charge redistribution on the CoP/TiO_x interface, CoP/TiO_x heterostructure model was constructed and DFT calculations were carried out (Figure S18, Supporting Information). Note that the surface of CoP in the CoP/TiO_x heterostructure model is oxidized. Charge density difference showed that strong charge redistribution appeared on the CoP/TiO_x interface region with electron accumulation and depletion near O and Co atoms, respectively (Figure 5A-C). The electron redistribution can modify the electronic structure and the adsorption energy of the reactant molecules of the active sites, leading to promoted reaction kinetics.^[6c-g,20] Modifying the water adsorption energy was proposed an important way to improve the OER reaction activity.^[10c] Figure 5D illustrates the optimized water adsorption configurations and energy on CoP and CoP-TiO_x. The water adsorption energy on CoP-TiO_x was -0.62, 0.05 eV lower than that of CoP (-0.57 eV), suggesting a better ability to adsorb water molecules and a higher OER activity of CoP-TiO_x than CoP.^[10c] 2) In addition to modification of the water molecule adsorption, the coupling of CoP with TiO_x also led to an improved charge transfer process as the Ti³⁺ sites (O vacancies) can endow TiO_x with metallic feature. It was evidenced

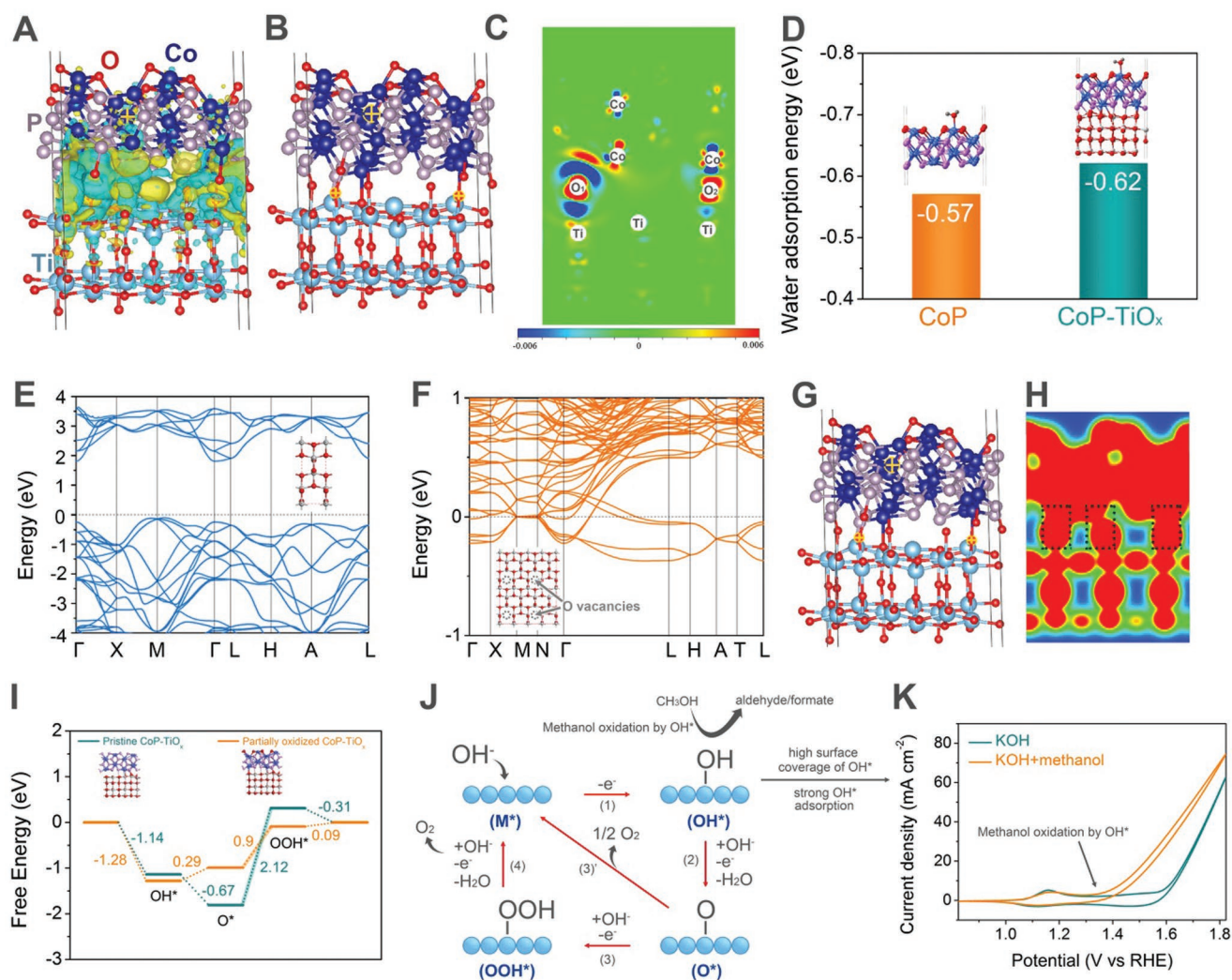


Figure 5. A) The charge density difference in the CoP/TiO_x interface of CoP–TiO_x. Yellow and blue areas represent electron accumulation and depletion, respectively. B) CoP–TiO_x heterostructure model and C) the corresponding charge density difference of the cross-section. Red and blue areas represent electron accumulation and depletion, respectively. D) Optimized structure of water molecular adsorption on CoP and CoP–TiO_x and the corresponding water adsorption energy. Band structures of E) TiO₂ and F) TiO_x with O vacancies (Ti³⁺ sites). G,H) Charge density of the cross section of CoP–TiO_x. The possible electron pathways on the CoP/TiO_x interfaces for fast electron transport is marked with dashed rectangle. I) Standard free energy diagram of the OER process at 1.23 V on the pristine CoP–TiO_x and partially oxidized CoP–TiO_x. J) Proposed mechanism of OER processes. K) Electrochemical response to methanol on CoP–TiO_x during OER process and the corresponding mechanism. CV curves were obtained using a scan rate of 20 mV s^{−1} without iR compensation.

by the band structures of TiO₂ and TiO_x with Ti³⁺ sites, which showed that TiO₂ had a semiconductive band structure with wide band gap while TiO_x with Ti³⁺ sites exhibited a metallic band structure (Figure 5E,F). Moreover, there showed electron pathways on the CoP/TiO_x interfaces for fast electron transport (Figure 5G,H). The improved charge transport of CoP coupled with TiO_x was evidenced by electrochemical impedance spectroscopy (EIS) measurements (Figure S19, Supporting Information). The Nyquist plots of CoP–TiO_x and CoP were composed of a semicircle at high frequency region and a straight line at low frequency region. The much smaller diameter of the semicircle and closer spike-like region to the imaginary axis for CoP–TiO_x than that for CoP indicated a much improved charge transfer kinetic by coupling CoP with TiO_x substrate.^[13c]

3) The robust TiO_x substrates in CoP–TiO_x can anchor the CoP nanoparticles and prevent their aggregation, resulting in high exposure of the active sites on the surface of the ultrafine CoP nanoparticles. In contrast, CoP obtained directly from ZIF-67 without TiO_x suffered from severe aggregation (Figure S20, Supporting Information). Moreover, the porous TiO_x shells with hollow structure can ensure the facile mass transport. 4) The compositional/structural evolution of CoP–TiO_x into partially oxidized CoP–TiO_x plays an important role to its desirable OER performance, which leads to a decreased rate-determining step (RDS) energy (Figure 5I). The RDSs of CoP–TiO_x and partially oxidized CoP–TiO_x are the formation of OOH* (reaction (3) in Figure 5J). The RDS (formation of OOH*) of pristine CoP–TiO_x has an energy barrier of 2.12 eV, which is

reduced to 0.9 eV after compositional/structural evolution of CoP–TiO_x into partially oxidized CoP–TiO_x. We applied a methanol-assistant method to in situ probe OER intermediates of CoP–TiO_x during OER process according to a reported work (Figure 5K).^[21] It was showed that after addition of methanol in KOH, a distinct oxidation current can be detected around the onset potential of OER, which can be attributed to the methanol oxidation by the OER intermediate OH*. The large methanol oxidation current indicated that CoP–TiO_x had a high surface coverage of OH* and thus the OER kinetics on CoP–TiO_x were limited by formation of O* (reaction (2)) or OOH* (reaction (3)). These results are consistent with the calculated results by DFT.

We also demonstrated the universality of the presented MOF-templated method was universal and can be applied to fabricate other phosphide/TiO_x heterostructures (Figures S21 and S22, Supporting Information).

3. Conclusion

In summary, CoP–TiO_x hybrid material with CoP/TiO_x heterostructure was fabricated using MOF nanocrystals as templates for efficient and durable OER electrocatalysis. The utilization of well-defined MOF nanocrystals leads to unique TiO_x hollow nanocage structures and uniform distribution of CoP nanoparticles. The introduction of the TiO_x hollow nanocages with abundant Ti³⁺ sites can not only prevent the aggregation of CoP nanoparticles, but also facilitate the electron transfer and mass transport. Moreover, the existence of abundant CoP/TiO_x interface in the resultant composite CoP–TiO_x greatly promoted the charge transport and modified the electron density of CoP for more efficient OER electrocatalysis. We believe this work will offer new design idea and provide a new route for the fabrications of efficient and durable electrocatalysts for OER electrocatalysis and many other electrochemical applications.

4. Experimental Section

Synthesis of ZIF-67: ZIF-67 nanocrystals with a particle size of ≈300 nm were synthesized through a coprecipitation method reported by the group of this work.^[7] Typically, 1.436 g of Co(NO₃)₂·6H₂O was dissolved into 100 mL of methanol to form solution A, while 3.244 g of 2-methylimidazole was dissolved into another 100 mL of methanol to form solution B. Then, solution A was poured into solution B under vigorous stir. The resultant mixture was kept stirred for 12 min and then kept standing for 24 h. Afterward, the ZIF-67 nanocrystals were separated by centrifugation and washed with ethanol for at least three times, followed by drying at 80 °C for 12 h.

Synthesis of ZIF-67–TiO_x: The ZIF-67 nanocrystals were coated with thin TiO_x shells using titanium butoxide as TiO_x source. Typically, 120 mg of the as-prepared ZIF-67 nanocrystals was dispersed into 60 mL of ethanol containing 0.3 mL of water through sonication. Afterward, 6 mL of ethanol containing 0.125 mL of titanium butoxide was added into the ZIF-67 suspension dropwise under vigorous stirring. The resulting mixture was heated to 80 °C and was kept for 90 min. Then the ZIF-67–TiO_x was separated by centrifugation and washed with ethanol for three times, followed by drying at 80 °C for 12 h.

Synthesis of Co₃O₄–TiO_x: Co₃O₄–TiO_x was obtained by pyrolysis of ZIF-67–TiO_x at 400 °C (1 °C min^{−1} ramping up to 400 °C) for 1 min in air.

Synthesis of CoP–TiO_x: CoP–TiO_x was obtained by phosphorization of Co₃O₄–TiO_x using NaH₂PO₂ as phosphorus source. Typically, 10 mg of the Co₃O₄–TiO_x powder was put into a small crucible, which was then put into a big crucible containing 100 mg of NaH₂PO₂·H₂O. The big crucible containing the small crucible was placed in a furnace and was kept at 350 °C (2 °C min^{−1} ramping up to 350 °C) for 2 h, and the final product CoP–TiO_x was obtained.

Synthesis of Co₃O₄ and CoP from ZIF-67 without TiO_x Shell: For comparison, Co₃O₄ and CoP were synthesized from ZIF-67 without TiO_x shells. To synthesize Co₃O₄, ZIF-67 nanocrystals were pyrolyzed at 400 °C (1 °C min^{−1} ramping up to 400 °C) for 1 min in air and Co₃O₄ was obtained. CoP was obtained by phosphorization of the as-prepared Co₃O₄: 10 mg of the Co₃O₄ powder was put into a small crucible, which was then put into a big crucible containing 100 mg of NaH₂PO₂·H₂O. The big crucible containing the small crucible was placed in a furnace and was kept at 350 °C (2 °C min^{−1} ramping up to 350 °C) for 2 h, and the CoP was obtained.

Synthesis of Co(OH)₂–TiO_x: For comparison Co(OH)₂–TiO_x hybrid material was fabricated using ZIF–TiO_x as precursor. Typically, 10 mg of ZIF–TiO_x was dispersed into 10 mL of ethanol by sonication. Afterward, 5 mL of Co(NO₃)₂·6H₂O ethanol solution (40 mg mL^{−1}) was injected into the ZIF–TiO_x suspension. The mixture was then sealed into 20 mL Teflon-lined autoclave. The reaction was carried out at 120 °C for 4 h (5 °C min^{−1} ramping up to 120 °C). The resultant pink powder was separated by centrifugation and washed with ethanol for three times and dried at 80 °C overnight to obtain the final Co(OH)₂–TiO_x product.

Synthesis of RuO₂ Nanoparticles: To fabricate RuO₂ nanoparticles as reference material to compare OER performance, Ru nanoparticles were first fabricated with a modified previously reported method.^[22] Then, the Ru nanoparticles were placed in a crucible was kept in a furnace at 500 °C (5 °C min^{−1} ramping up to 500 °C) for 12 h to obtain RuO₂ nanoparticles.

Synthesis of IrO₂ Nanoparticles: IrO₂ nanoparticles were fabricated as reference material to compare OER performance according to a reported work.^[23]

Synthesis of MIL-88B-NH₂: MIL-88B-NH₂ rod-like nanocrystals were synthesized through a modified method reported previously.^[24] Typically, 0.96 g of F127 was dissolved into 80 mL of water and 10 mL of 0.4 M FeCl₃ solution was injected into the F127 solution. The resulting solution was kept stirring for 2 h. Afterward, 1.8 mL of CH₃COOH was injected and the solution was kept stirring for another 2 h. The 0.36 g of 2-aminoterephthalic acid was added and the solution was kept stirring for additional 2 h. The resulting mixture was sealed into Teflon-lined autoclave and was kept at 110 °C for 24 h. The resulting MIL-88B-NH₂ powder was centrifugated and washed by ethanol for three times.

Synthesis of Ni-BTC: Ni-BTC sphere-like nanocrystals were synthesized through a previously reported method.^[25] Typically, 108 mg of Ni(acac)₂, 33.6 mg of H₃BTC, and 200 mg of PVP were dissolved into a mixture solution (32 mL of DMF and 20 mL of ethyl glycol), which were then sealed in a 100 mL Teflon-lined autoclave and kept at 180 °C for 3 h. The resulting Ni-BTC powder was centrifugated and washed by ethanol for three times.

Synthesis of MIL-88B-NH₂–TiO_x and Ni-BTC–TiO_x: The MOF (MIL-88B-NH₂ and Ni-BTC) nanocrystals were coated with thin TiO_x shells using titanium butoxide as TiO_x source. Typically, 120 mg of the as-prepared MOF nanocrystals were dispersed into 60 mL of ethanol containing 0.3 mL of water through sonication. Afterward, 6 mL of ethanol containing 0.125 mL of titanium butoxide was added into the MOF suspension dropwise under vigorous stirring. The resulting mixture was heated to 80 °C and was kept for 90 min. Then, the MOF–TiO_x was separated by centrifugation and washed with ethanol for three times, followed by drying at 80 °C for 12 h.

Synthesis of Ni₂P–TiO_x and FeP–TiO_x: Ni₂P–TiO_x was synthesized using a similar method except that Ni-BTC–TiO_x rather than ZIF-67–TiO_x was used as precursor. For FeP–TiO_x, MIL-88B-NH₂–TiO_x was used as precursor and the phosphorization temperature was 500 °C.

Characterization: XRD patterns were measured by Rigaku Corporation SmartLab 9 kW at 45 kV and 200 mA using Cu Kα radiation. SEM

images were obtained on a Hitachi S-4800 microscope. TEM images were obtained using a transmission electron microscope (Hitachi, H-9000NAR). HRTEM was measured using an FEI Tecnai F30 microscope. XPS was measured by X-ray photoelectron spectroscopy (XPS, Axis Ultra, Kratos Analytical, Japan) with monochromatic aluminum K α as source of X-ray.

Electrochemical Measurements: The electrochemical measurements were carried out on a CHI 760E electrochemical workstation using a standard three-electrode system with catalyst-modified glassy carbon electrode, KCl saturated Ag/AgCl electrode, and Pt foil as working electrode, reference electrode, and counter electrode, respectively. 1 M KOH saturated with O₂ was used as electrolyte. To prepare catalyst-modified glassy carbon electrode, 2 mg of catalyst was dispersed into 1 mL of ethanol containing 10 μ L of 5 wt% Nafion by sonication for a least 1 h, and 20 μ L of the resulting ink was then loaded on the glassy carbon electrode with diameter of 5 mm (catalyst loading of \approx 0.2 mg cm⁻²). The potentials in this paper is referred to reversible hydrogen electrode (RHE) using $E_{\text{RHE}} = E_{\text{Ag/AgCl}} + 0.197 \text{ V} + 0.059 \text{ pH}$. The LSV curves were obtained at scan rate of 5 mV s⁻¹. For RRDE measurements, RRDE with glassy carbon disk and Pt ring (PINE E6 RRDE) was used. For durability tests, carbon fiber paper with geometrical area of 1 cm² was used to support the catalysts as recommended in order to reveal the available durability of the catalysts for large-scale water electrolysis.

For electrochemical surface area (ECSA) normalized current density, ESCA was estimated by measuring the electrical double-layer capacitance (C_{dl}).^[26] C_{dl} was obtained according to the equation

$$C_{\text{dl}} = \frac{\Delta J}{2\nu} \quad (1)$$

where ΔJ is equal to J_{anode} minus J_{cathode} , and ν is the potential scan rate. ΔJ and ν were obtained by cycling the electrodes in the non-Faradaic potential regions (-0.7 to -0.3 V vs KCl-saturated Ag/AgCl) in nitrogen-saturated 1 M KOH in order to minimize the oxygen reduction reaction. Because of the linear slopes, the C_{dl} values can be estimated by the slopes in Figure 3C. Then, the roughness factor was calculated by the equation

$$\text{ECSA} = \frac{C_{\text{dl}}}{C_s} \quad (2)$$

where C_s is the specific capacitance of electrode with smooth planar surface. C_s of 0.040 mF cm⁻² was used according to the reported literatures.^[27] Then, the current densities of the samples were normalized by ECSA value according to the equation (Figure 3D)

$$J_{\text{ECSA}} = \frac{J}{\text{ECSA}} \quad (3)$$

where J is the current density based on geometrical surface area of the electrode (0.19625 cm²).

Theoretical Calculations: All calculations were performed based on density functional theory (DFT) implemented in the Vienna Ab Initio Simulation Package (VASP).^[28] The projector augmented wave (PAW) method^[29] was used to treat the interactions between ion cores and valence electrons. The exchange-correlation potential was incorporated by using the generalized gradient approximation (GGA) in the Perdew–Burke–Ernzerhof (PBE) form.^[30] Plane waves with a kinetic energy cutoff of 400 eV were used to expand valence electron wavefunctions. Monkhorst–Pack k -meshes^[31] of $10 \times 10 \times 4$ for TiO₂ unit cell, $2 \times 10 \times 2$ for TiO₂ supercell ($4 \times 2 \times 1$) and $2 \times 3 \times 1$ for CoP/ TiO₂ heterostructure, and CoP slab were used. All studied structures were fully relaxed until the energy and force on each atom were less than 0.0001 eV and 0.01 eV \AA^{-1} , respectively.

In order to study the charge redistribution on the CoP/TiO_x interface, a 2D CoP–TiO₂ heterostructure was constructed, and then one O atom was removed from the CoP/TiO₂ heterostructure to mimic the CoP/TiO_x interface with defects. The details are given in Figure S13 (Supporting

Information). The vacuum space of 12 \AA in the z-direction was set to prevent the interaction between the periodic images. The adsorption energy of H₂O molecule on the surfaces was calculated by using the below equation

$$E_{\text{ads}} = E_{*-\text{H}_2\text{O}} - E_* - E_{\text{H}_2\text{O}} \quad (4)$$

where $E_{*-\text{H}_2\text{O}}$ is the total energy of the CoP slab or the CoP–TiO_x heterostructure with H₂O molecule adsorbed on the Co site, E_* is the total energy of the CoP slab or the CoP/ TiO_x heterostructure, and $E_{\text{H}_2\text{O}}$ is the total energy of an isolated H₂O.

Supporting Information

Supporting Information is available from the Wiley Online Library or from the author.

Acknowledgements

Z.L. and W.Z. contributed equally to this work. This work was financially supported by the Natural Science Foundation of China (518205201), the National Key Research and Development Program of China (2017YFA0206701), National Program for Support of Top-Notch Young Professionals, and Changjiang Scholar Program.

Conflict of Interest

The authors declare no conflict of interest.

Keywords

cobalt phosphide, heterostructures, oxygen evolution reaction, synergistic effect, titanium oxide

Received: September 5, 2019

Revised: October 29, 2019

Published online:

- [1] a) M. Tahir, L. Pan, F. Idrees, X. Zhang, L. Wang, J.-J. Zou, Z. L. Wang, *Nano Energy* **2017**, *37*, 136; b) Z.-F. Huang, J. Song, Y. Du, S. Xi, S. Dou, J. M. V. Nsanzimana, C. Wang, Z. J. Xu, X. Wang, *Nat. Energy* **2019**, *4*, 329; c) N.-T. Suen, S.-F. Hung, Q. Quan, N. Zhang, Y.-J. Xu, H. M. Chen, *Chem. Soc. Rev.* **2017**, *46*, 337; d) Z. Liang, W. Guo, R. Zhao, T. Qiu, H. Tabassum, R. Zou, *Nano Energy* **2019**, *64*, 103917.
- [2] a) I. Roger, M. A. Shipman, M. D. Symes, *Nat. Rev. Chem.* **2017**, *1*, 0003; b) T. Qiu, Z. Liang, W. Guo, S. Gao, C. Qu, H. Tabassum, H. Zhang, B. Zhu, R. Zou, Y. Shao-Horn, *Nano Energy* **2019**, *58*, 1.
- [3] a) Z. Liang, R. Zhao, T. Qiu, R. Zou, Q. Xu, *EnergyChem* **2019**, *1*, 100001; b) F. Lu, M. Zhou, Y. Zhou, X. Zeng, *Small* **2017**, *13*, 1701931; c) J. Nai, H. Yin, T. You, L. Zheng, J. Zhang, P. Wang, Z. Jin, Y. Tian, J. Liu, Z. Tang, L. Guo, *Adv. Energy Mater.* **2015**, *5*, 1401880; d) W. Zhou, L. Guo, *Chem. Soc. Rev.* **2015**, *44*, 6697.
- [4] a) X. Xiao, C.-T. He, S. Zhao, J. Li, W. Lin, Z. Yuan, Q. Zhang, S. Wang, L. Dai, D. Yu, *Energy Environ. Sci.* **2017**, *10*, 893; b) W. Li, X. Gao, D. Xiong, F. Xia, J. Liu, W.-G. Song, J. Xu, S. M. Thalluri, M. F. Cerqueira, X. Fu, L. Liu, *Chem. Sci.* **2017**, *8*, 2952; c) D. Li, H. Baydoun, C. N. Verani, S. L. Brock, *J. Am. Chem. Soc.* **2016**, *138*, 4006.

- [5] a) K. Xu, H. Cheng, L. Liu, H. Lv, X. Wu, C. Wu, Y. Xie, *Nano Lett.* **2017**, *17*, 578; b) M. Liu, J. Li, *ACS Appl. Mater. Interfaces* **2016**, *8*, 2158.
- [6] a) C. G. Morales-Guio, E. R. Cave, S. A. Nitopi, J. T. Feaster, L. Wang, K. P. Kuhl, A. Jackson, N. C. Johnson, D. N. Abram, T. Hatsukade, C. Hahn, T. F. Jaramillo, *Nat. Catal.* **2018**, *1*, 764; b) J. Lai, B. Huang, Y. Tang, F. Lin, P. Zhou, X. Chen, Y. Sun, F. Lv, S. Guo, *Chem* **2018**, *4*, 1153; c) L. An, Z. Zhang, J. Feng, F. Lv, Y. Li, R. Wang, M. Lu, R. B. Gupta, P. Xi, S. Zhang, *J. Am. Chem. Soc.* **2018**, *140*, 17624; d) J. Azadmanjiri, V. K. Srivastava, P. Kumar, M. Nikzad, J. Wang, A. Yu, *J. Mater. Chem. A* **2018**, *6*, 702; e) R. Subbaraman, D. Tripkovic, D. Strmcnik, K.-C. Chang, M. Uchimura, A. P. Paulikas, V. Stamenkovic, N. M. Markovic, *Science* **2011**, *334*, 1256; f) Z. Zhuang, Y. Li, Z. Li, F. Lv, Z. Lang, K. Zhao, L. Zhou, L. Moskaleva, S. Guo, L. Mai, *Angew. Chem., Int. Ed.* **2018**, *57*, 496; g) J. Xu, T. Liu, J. Li, B. Li, Y. Liu, B. Zhang, D. Xiong, I. Amorim, W. Li, L. Liu, *Energy Environ. Sci.* **2018**, *11*, 1819.
- [7] W. Xia, J. Zhu, W. Guo, L. An, D. Xia, R. Zou, *J. Mater. Chem. A* **2014**, *2*, 11606.
- [8] H. Yang, P. E. Kruger, S. G. Telfer, *Inorg. Chem.* **2015**, *54*, 9483.
- [9] W. Wang, M. Dahl, Y. Yin, *Chem. Mater.* **2013**, *25*, 1179.
- [10] a) J. Lai, B. Huang, Y. Tang, F. Lin, P. Zhou, X. Chen, Y. Sun, F. Lv, S. Guo, *Chem* **2018**, *4*, 1153; b) P. Wang, X. Zhang, J. Zhang, S. Wan, S. Guo, G. Lu, J. Yao, X. Huang, *Nat. Commun.* **2017**, *8*, 14580; c) Y. Zhao, X. Jia, G. Chen, L. Shang, G. I. N. Waterhouse, L.-Z. Wu, C.-H. Tung, D. O'Hare, T. Zhang, *J. Am. Chem. Soc.* **2016**, *138*, 6517; d) Z. H. Xue, H. Su, Q. Y. Yu, B. Zhang, H. H. Wang, X. H. Li, J. S. Chen, *Adv. Energy Mater.* **2017**, *7*, 1602355.
- [11] a) X. Yu, S. Zhang, C. Li, C. Zhu, Y. Chen, P. Gao, L. Qi, X. Zhang, *Nanoscale* **2016**, *8*, 10902; b) H. Tabassum, W. Guo, W. Meng, A. Mahmood, R. Zhao, Q. Wang, R. Zou, *Adv. Energy Mater.* **2017**, *7*, 1601671; c) Z. Liang, C. Qu, W. Zhou, R. Zhao, H. Zhang, B. Zhu, W. Guo, W. Meng, Y. Wu, W. Aftab, Q. Wang, R. Zou, *Adv. Sci.* **2019**, 1802005.
- [12] Y. Liu, Y. Zhu, J. Shen, J. Huang, X. Yang, C. Li, *Nanoscale* **2018**, *10*, 2603.
- [13] a) X. Lu, G. Wang, T. Zhai, M. Yu, J. Gan, Y. Tong, Y. Li, *Nano Lett.* **2012**, *12*, 1690; b) X. Lu, M. Yu, G. Wang, T. Zhai, S. Xie, Y. Ling, Y. Tong, Y. Li, *Adv. Mater.* **2013**, *25*, 267; c) Q. Ke, C. Guan, X. Zhang, M. Zheng, Y. W. Zhang, Y. Cai, H. Zhang, J. Wang, *Adv. Mater.* **2017**, *29*, 1604164.
- [14] S. Zhao, Y. Wang, J. Dong, C.-T. He, H. Yin, P. An, K. Zhao, X. Zhang, C. Gao, L. Zhang, J. Lv, J. Wang, J. Zhang, A. M. Khattak, N. A. Khan, Z. Wei, J. Zhang, S. Liu, H. Zhao, Z. Tang, *Nat. Energy* **2016**, *1*, 16184.
- [15] S. Anantharaj, S. R. Ede, K. Karthick, S. Sam Sankar, K. Sangeetha, P. E. Karthik, S. Kundu, *Energy Environ. Sci.* **2018**, *11*, 744.
- [16] a) Y. P. Zhu, Y. P. Liu, T. Z. Ren, Z. Y. Yuan, *Adv. Funct. Mater.* **2015**, *25*, 7337; b) L.-A. Stern, L. Feng, F. Song, X. Hu, *Energy Environ. Sci.* **2015**, *8*, 2347.
- [17] G. Zhang, G. Wang, Y. Liu, H. Liu, J. Qu, J. Li, *J. Am. Chem. Soc.* **2016**, *138*, 14686.
- [18] J. Ryu, N. Jung, J. H. Jang, H.-J. Kim, S. J. Yoo, *ACS Catal.* **2015**, *5*, 4066.
- [19] Z. H. Xue, J. T. Han, W. J. Feng, Q. Y. Yu, X. H. Li, M. Antonietti, J. S. Chen, *Angew. Chem.* **2018**, *130*, 2727.
- [20] Y. Liu, Q. Li, R. Si, G.-D. Li, W. Li, D.-P. Liu, D. Wang, L. Sun, Y. Zhang, X. Zou, *Adv. Mater.* **2017**, *29*, 1606200.
- [21] H. B. Tao, Y. Xu, X. Huang, J. Chen, L. Pei, J. Zhang, J. G. Chen, B. Liu, *Joule* **2019**, *3*, 1498.
- [22] J. Su, Y. Yang, G. Xia, J. Chen, P. Jiang, Q. Chen, *Nat. Commun.* **2017**, *8*, 14969.
- [23] G. Li, S. Li, M. Xiao, J. Ge, C. Liu, W. Xing, *Nanoscale* **2017**, *9*, 9291.
- [24] M.-H. Pham, G.-T. Vuong, A.-T. Vu, T.-O. Do, *Langmuir* **2011**, *27*, 15261.
- [25] H. Yang, B. Wang, H. Li, B. Ni, K. Wang, Q. Zhang, X. Wang, *Adv. Energy Mater.* **2018**, *8*, 1801839.
- [26] D. Voiry, M. Chhowalla, Y. Gogotsi, N. A. Kotov, Y. Li, R. M. Penner, R. E. Schaak, P. S. Weiss, *ACS Nano* **2018**, *12*, 9635.
- [27] a) C. C. L. McCrory, S. Jung, J. C. Peters, T. F. Jaramillo, *J. Am. Chem. Soc.* **2013**, *135*, 16977; b) C. Luan, G. Liu, Y. Liu, L. Yu, Y. Wang, Y. Xiao, H. Qiao, X. Dai, X. Zhang, *ACS Nano* **2018**, *12*, 3875.
- [28] G. Kresse, J. Furthmüller, *Phys. Rev. B* **1996**, *54*, 11169.
- [29] P. E. Blöchl, *Phys. Rev. B* **1994**, *50*, 17953.
- [30] J. P. Perdew, K. Burke, M. Ernzerhof, *Phys. Rev. Lett.* **1996**, *77*, 3865.
- [31] H. J. Monkhorst, J. D. Pack, *Phys. Rev. B* **1976**, *13*, 5188.